

## Calorimetric investigations in a gas aggregation source

Sven Gauter, Fabian Haase, Pavel Solař, Ondřej Kylián, Peter Kúš, Andrei Choukourov, Hynek Biederman, and Holger Kersten

Citation: *Journal of Applied Physics* **124**, 073301 (2018); doi: 10.1063/1.5037413

View online: <https://doi.org/10.1063/1.5037413>

View Table of Contents: <http://aip.scitation.org/toc/jap/124/7>

Published by the [American Institute of Physics](#)

---

### Articles you may be interested in

Tutorial: [Organic field-effect transistors: Materials, structure and operation](#)

*Journal of Applied Physics* **124**, 071101 (2018); 10.1063/1.5042255

[Investigation of the thermal stability of MoO<sub>x</sub> as hole-selective contacts for Si solar cells](#)

*Journal of Applied Physics* **124**, 073106 (2018); 10.1063/1.5041774

[Effects of surface roughness on surface charge accumulation characteristics and surface flashover performance of alumina-filled epoxy resin spacers](#)

*Journal of Applied Physics* **124**, 083302 (2018); 10.1063/1.5043239

[High temperature magnetic studies on Bi<sub>1-x</sub>Ca<sub>x</sub>Fe<sub>1-y</sub>Ti<sub>y</sub>O<sub>3-δ</sub> nanoparticles: Observation of Hopkinson-like effect above T<sub>N</sub>](#)

*Journal of Applied Physics* **124**, 073904 (2018); 10.1063/1.5038007

[Broadband optical response of graphene measured by terahertz time-domain spectroscopy and FTIR spectroscopy](#)

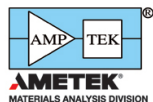
*Journal of Applied Physics* **124**, 073105 (2018); 10.1063/1.5044265

[Cryogenic optomechanic cavity in low mechanical loss material](#)

*Journal of Applied Physics* **124**, 073104 (2018); 10.1063/1.5042058

---

## Ultra High Performance SDD Detectors



See all our XRF Solutions

## Calorimetric investigations in a gas aggregation source

Sven Gauter,<sup>1</sup> Fabian Haase,<sup>1</sup> Pavel Solař,<sup>2</sup> Ondřej Kylián,<sup>2</sup> Peter Kúš,<sup>3</sup> Andrei Choukourov,<sup>2</sup> Hynek Biederman,<sup>2</sup> and Holger Kersten<sup>1</sup>

<sup>1</sup>*Institute of Experimental and Applied Physics, Kiel University, Kiel, Germany*

<sup>2</sup>*Department of Macromolecular Physics, Faculty of Mathematics and Physics, Charles University, Prague, Czech Republic*

<sup>3</sup>*Department of Surface and Plasma Science, Faculty of Mathematics and Physics, Charles University, Prague, Czech Republic*

(Received 24 April 2018; accepted 30 July 2018; published online 21 August 2018)

A gas aggregation source based on DC magnetron sputtering was investigated using a passive thermal probe and supplementary diagnostics (Langmuir probe and quartz crystal microbalance). Parameter variations of pressure, axial distance, and magnetron current have been performed for three different targets (pure Cu, pure W, composite Cu/W) in argon discharge. The measurements showed the energy flux to be significantly higher for the case of the pure tungsten and the composite target compared to the copper target, which is likely a result of the strongly increased amount of neutrals being reflected from the heavier targets. Furthermore, gas rarefaction by the sputtered atoms was found to be essential for the understanding of the observed energy flux and that the dominant contributors to the energy flux in the higher pressure regime are comparable to those observed in the conventional lower pressure regime. Selected deposited films have been investigated *ex-situ* by scanning electron microscopy, which allowed us to gain insight into the nanoparticle formation in relation to the observed energy conversion. *Published by AIP Publishing.*  
<https://doi.org/10.1063/1.5037413>

### I. INTRODUCTION

Metal nanoparticles (NPs) produced by means of gas aggregation cluster sources (GAS) represent an ever growing field in nanoscience.<sup>1–5</sup> In the past, the major focus was laid upon the construction of GAS themselves,<sup>6,7</sup> to understand the basic principles of the nanoparticle formation process,<sup>1,2,8,9</sup> the properties of single-phase particles, and their transport to substrates.<sup>10–12</sup> Recent developments shift the focus from a single material to composite nanoparticles, which resulted in a variety of different approaches to achieve complex nanoparticle formation. Some methods employ multiple steps such as in-flight coating or subsequent coating of single-metal NPs by a thin film of another material.<sup>13,14</sup> Although the formation of the core is in this case completely decoupled from the deposition of the shell, the produced shell is usually very thin (typically several nm). Another method utilizes simultaneous sputtering of two or more metals from several magnetrons in one aggregation chamber<sup>15</sup> allowing for the production of multi-component NPs. Although control of the component ratio can be well achieved with this method, the control of the overall homogeneity is not straightforward. The same problem arises when a single magnetron is used with a target composed of two halves consisting of two different metals.<sup>16,17</sup> Other studies with different forms of composite targets like a silver target with a concentric thin gold wire inserted in the erosion track<sup>18</sup> or various alloyed targets<sup>19–21</sup> were found to reliably produce nanoparticles with varying results regarding particle size distribution, composition, and structure. A similar approach, which is investigated in this study, is based on small pellets of different materials located in the erosion

track. Although the possibility to produce core-shell NPs using this method was already demonstrated,<sup>22</sup> the formation and growth of such NPs is still not well-understood. This is partially due to insufficient knowledge of the processes occurring inside the aggregation chamber, such as heating/cooling of growing NPs. To gain insight into the energy flux inside the aggregation chamber and, thus, also on the energy conversion relevant for the formation process of the particles, energy flux measurements using a passive thermal probe (PTP) were performed for different settings of discharge power, gas pressure, and distance to target. Supplementary to the measurement of the power density (energy flux) with the PTP, the deposition rate was measured using a quartz crystal microbalance (QCM), and plasma parameters were monitored with a Langmuir probe (LP). To correlate the obtained experimental values with the formation process of the particles, these test films were deposited for selected parameter sets and analyzed using a scanning electron microscope (SEM).

### II. EXPERIMENTAL SETUP OF THE GAS

The investigated system represents a typical gas aggregation cluster source consisting of an indirectly cooled 3 in. magnetron inserted on the axis of a cylindrical vacuum chamber of 100 mm diameter. The distance between the target and the exit orifice (2 mm diameter) was 131 mm for the standard magnetron position (distance magnetron to PTP: 16 mm). To allow extraction of particles, the aggregation chamber is connected to the main, differentially pumped vacuum chamber ( $p < 1$  Pa, 210 l/s from turbo pump). The operation pressures of 20–210 Pa inside the aggregation

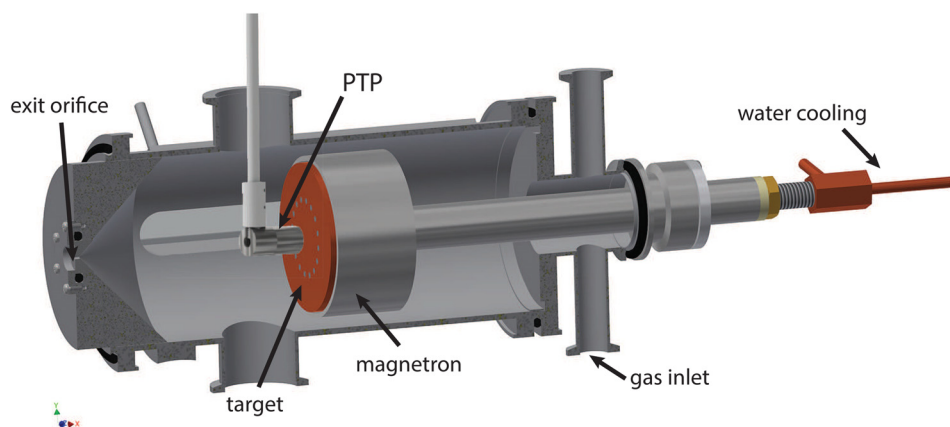


FIG. 1. Schematic drawing of the aggregation chamber. The probes were mounted inside the aggregation chamber at a standard distance of 16 mm from the magnetron.

chamber were obtained with a gas flow of 2–40 sccm of argon introduced at the top of the chamber (see Fig. 1). Differential pumping creates a pressure gradient directed from the gas input of the aggregation chamber towards its exit orifice, allowing efficient transport of clusters and particles. Both the magnetron and the chamber walls were cooled with water. The position of the magnetron in the chamber was adjustable via a sliding vacuum feedthrough, see Fig. 1. The magnetron was powered by an *Advanced Energy MDX500* DC power supply operated in constant current mode. The magnetron voltage, current, and power were continuously recorded to monitor the process. Pure Ar was used as a process gas.

For all measurements, the probes were side-mounted to the aggregation chamber facing the magnetron target. Since the probes could not be moved along the vertical axis of the magnetron, the distance variation was performed by moving the magnetron to the most distant position ( $d_{max} = 66$  mm) and then successively moving it closer to the probes with intermittent measurements until reaching the minimum distance of  $d_{min} = 16$  mm.

Identical parameter variations as summarized in Table I have been performed for three different targets: a pure tungsten target, a pure copper target, and a composite target made from copper with 37 tungsten pellets of 3 mm diameter distributed over the race track (see Fig. 2). All targets were 3 mm in thickness and exhibited similar erosion depths in the race track area. To identify systematic errors such as time-dependent changes in the surface condition of the target, several parameter settings have been measured twice at different times during the variation. The resulting deviation is represented as error bars in the presented measurement results.

TABLE I. Experimental parameters used for the parameter variations performed for three different targets, with the varied values printed **bold**. All experiments were performed with argon and the magnetron was operated in current regulated mode. The standard condition was chosen to be at 16 mm distance to the target, 500 mA current, and 60 Pa pressure.

	Variation of distance	Variation of current	Variation of pressure
Distance (mm)	<b>16–66</b>	16	16
Current (mA)	500	<b>50–500</b>	500
Pressure (Pa)	60	60	<b>20–210</b>

### III. UTILIZED PROBES

All measurements were performed subsequently with three different kinds of probes centered on the chamber and magnetron axis at approximately the same distance to the target. The Langmuir probe measurements were performed using the PTP substrate as a planar Langmuir probe which was biased using a copper wire. The corresponding plasma parameters were primarily calculated to allow an estimation of the energy flux by ions and electrons and are, thus, not discussed in greater detail in this study.

#### A. Quartz crystal microbalance

For the measurement of the deposition rate, a commercially available quartz crystal microbalance (QCM) *IL150* from *Intelmetrics Global Ltd* with a gold coated 14 mm diameter crystal without water cooling has been used. As described in Sec. II, the QCM was introduced to the chamber using the same mount as used for the PTP. Due to the different probe geometry, the QCM sensor was positioned at a slightly farther distance of 20 mm to the target surface at standard position. Since the QCM detects the change of mass on the quartz crystal, it is necessary to provide material specific constants to allow the calculation of the deposition rate in nm/min.<sup>23</sup> Since the determined deposition rate calculated from the change of mass is directly proportional to the assumed film density that has been set as an input parameter in the IL 150, it is necessary to obtain realistic densities for the different utilized targets. This was achieved by performing test depositions at different parameters allowing us to deduce effective densities from thickness and weight measurements. The resulting densities which were used for the determination of the deposition rates presented in Sec. IV A are summarized in Table II. It should be noted that the measured densities are lower as compared to the values of bulk



FIG. 2. Photograph of the utilized Cu/37W (left) and pure Cu (right) 3 in. targets used in the gas aggregation source. The pure W target is not shown.

TABLE II. Experimentally determined film densities for the three investigated targets.

Target material	Density (g/cm <sup>3</sup> )	
	Bulk	Determined
Composite (Cu/37W)		11.4 ± 0.9
Copper	8.96	7.4 ± 0.6
Tungsten	19.3	11.4 ± 0.8

metals which is due to the highly porous character of deposited nanoparticle films.

Although the determined densities from these test depositions showed relatively small errors, later depositions with different substrate holder configurations or substrate material showed strongly deviating results. For this reason, the results of the QCM are only evaluated regarding their relative changes for each investigated target. Here it should be noted that the change of film density for the different investigated conditions will result in somewhat erroneous deposition rates. However, this effect is expected to be small compared to the general trends and is not further considered for the sake of simplicity.

## B. Passive thermal probe

For the energy flux measurements inside the aggregation chamber, a passive thermal probe was side-mounted at a distance of 16 mm to the magnetron target and facing the target (see Fig. 1). A detailed description of this probe and the evaluation of the measurement are presented here as the understanding of the procedure is important for the discussion of the results in Sec. IV. The probe utilized in the experiments consists of a sensor plate (substrate dummy) made of copper with a diameter of 11 mm and a thickness of 70 μm. Spot-welded to the back of it is a Type K thermocouple and an additional copper wire for biasing and current readings.<sup>24</sup> The sensor plate is surrounded by a metallic shielding to make sure that only contributions from the upper half-space are considered. A schematic drawing of the PTP design is shown in Fig. 3.

It should be noted that the PTP always measures a time-averaged and integrated energy flux that is generated by various energy sources and processes such as charged and neutral particles, and surface processes like film formation or radiation from a hot target or chamber walls, respectively. The basic idea of the PTP is to calculate the energy flux from the relation between the time derivative of the enthalpy ( $\dot{H}$ ) and the time derivative of the temperature ( $\dot{T}_s$ ) of a well-defined substrate dummy. During the heating ( $T_h$ —energy source on) and the cooling ( $T_c$ —energy source off) of the substrate dummy, this relation yields

$$\text{Heating: } \dot{H}_h = C_s \dot{T}_h = P_{in} - P_{out,h}, \quad (1)$$

$$\text{Cooling: } \dot{H}_c = C_s \dot{T}_c = -P_{out,c}. \quad (2)$$

Here,  $C_s$  is the heat capacity of the probe,  $P_{in}$  gives the power from the source, and  $P_{out,h}$  and  $P_{out,c}$  denote the power leaving the probe during heating and cooling, respectively.

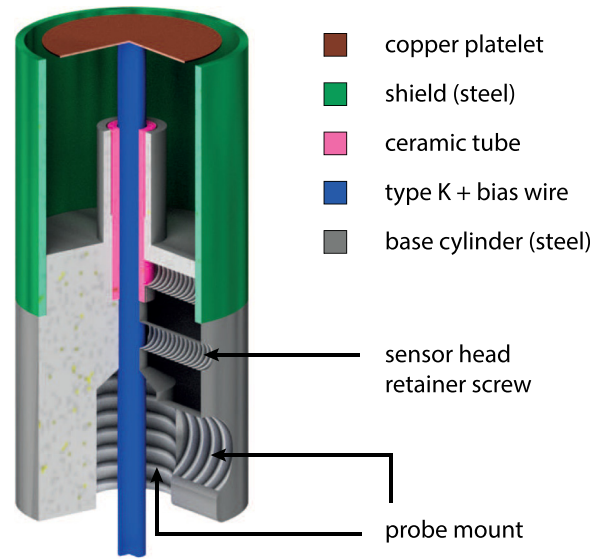


FIG. 3. Schematic drawing of the PTP sensor head. The Type K thermocouple and the bias wire are spot-welded to the back of the copper platelet that represents the substrate. The whole sensor is housed in a stainless steel cylinder to shield it from any surrounding influences other than the ones coming from the upper half-space.

Assuming that the negative cooling terms of Eqs. (1) and 2 are equal for the same substrate temperatures ( $P_{out,h}(T_s) = P_{out,c}(T_s)$ ), the equations for heating and cooling can be combined to calculate the energy flux  $J_{in}$

$$J_{in} = \frac{P_{in}}{A_s} = \frac{C_s}{A_s} (\dot{T}_h - \dot{T}_c). \quad (3)$$

There are several different methods of evaluating calorimetric temperature curves; however, if the power source is capable of fast switching between off- and on-states, the most desirable method is the so-called *kink method*. The main reason for this is that for the assumption of equal cooling terms during the heating and the cooling phase, any energy flux originating from secondary heat sources has to be constant for the investigated time period. When evaluating with the *kink method*, as described in Ref. 25, only a short time period of about 2 s around the kinks between the cooling and heating phases is evaluated. This means that the above-mentioned assumption only needs to apply in this short time frame. Accordingly, any contribution to the energy flux which is relatively constant during this time period does not significantly influence the measured energy flux. Through different measurement procedures, this allows us to eliminate certain effects from the measurement results. For example in the case investigated in this study, the contribution from target radiation does not appear in the measurement since the target temperature can be assumed to be approximately constant during the short measurement time of a few seconds. If instead the probe would be turned away on plasma shut-off or if a cooled shutter is used to shut off the energy flux, the target radiation would be included in the measurement.

The kink that evolves when switching the power source on from an off-state is referred to as heating kink and the kink that is created when the power source is switched off

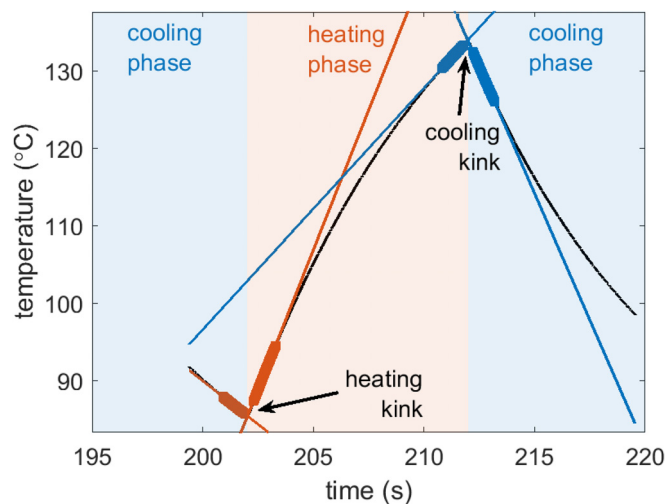


FIG. 4. Exemplary evaluation of a PTP curve with heating and cooling kinks. The highlighted areas in red and blue denote the data points that were used for the linear fits.

again, and the next cooling phase starts, is referred to as cooling kink. From both kinks, an accurate measurement of the energy flux at these times is obtained and any potential discrepancy between those two results can already be a valuable hint for the stability of the investigated process and the reliability of the measurement method. In Fig. 4, an exemplary temperature curve with clearly labeled cooling and heating phases as well as evaluated points and corresponding linear fits around the kinks are presented.

By subtracting the slopes of the two linear fits around the kinks,  $\dot{T}_h - \dot{T}_c$  can be easily obtained and the energy flux can be calculated from Eq. (3), using the heat capacity  $C_s$  and surface area  $A_s$  of the probe. The heat capacity was determined before and after the measurement campaign using a calibration experiment introduced in Ref. 24. The obtained values  $C_{s,before} = 0.027$  J/K and  $C_{s,after} = 0.036$  J/K show a significant deviation which is a result of the film deposited on the probe surface through the course of the measurement campaign. Figure 5 shows a microscopic photograph of the cross section of this film onto the PTP, where the temporal sequence of the measurements is mirrored by the color of the coating; first the copper target was investigated, second the composite target, and last the pure tungsten.

To compensate for the gradual increase in the heat capacity, for each variation, the value used for the evaluation of the PTP data was approximated by an interpolation taking into account the time the probe was exposed to the plasma, e.g., for the data from the first variation (distance-Cu), the

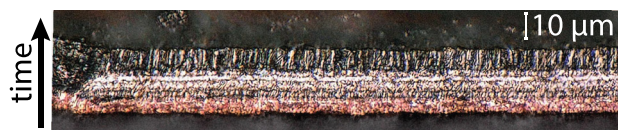


FIG. 5. Photograph of the deposited film on the PTP after the measurement campaign. The film was broken off from the probe and investigated under a microscope. Note the copper layer at the bottom exhibiting a somewhat grainy growth structure, followed by the film deposited with the composite target (middle layer) and the top tungsten layer, which exhibits a more columnar growth structure.

initial value of 0.027 J/K was used, for the variation in the middle (e.g., pressure-Cu/37W), an adjusted value of 0.030 J/K was used, and for the last variation (pressure-W) the final value of 0.036 J/K was used.

## IV. RESULTS AND DISCUSSION

A summary of the results obtained with the QCM and the PTP together with the corresponding values of the magnetron power is presented in Fig. 6. In Sec. IV, these complex correlations will be described along the discussion focused on the calorimetric results using QCM and Langmuir data to gain insights into the composition of the energy flux. The SEM images are used to provide a concrete connection between the measured values and the nanoparticle growth and are shortly discussed at the end of this section.

### A. Deposition rate

The trends for the deposition rate, which were obtained for the parameter variations introduced in Table I, are shown in the second row of Fig. 6. Here, we observe an almost linear trend for the distance- and the magnetron current variation, while the pressure variation exhibits a somewhat more complex dependence.

In a simple model, the deposition rate is mostly defined by two basic processes: (i) the production of sputtered atoms and (ii) the transport of sputtered atoms. The production of sputtered atoms depends on the sputter yield  $\gamma_s$  and the amount of species (energetic ions and neutrals) impinging on the target surface. A characteristic value which can be associated with the latter quantity is the magnetron current since it is approximately proportional to the amount of kinetic species arriving at the target surface. The sputter yield can be expected to be a function of the mass ratio between target and impinging species as well as of the energy of the impinging particles. This dependence has been investigated and semi-empirically described by many groups; however, especially for the lower energy range, still no universally accepted model is available.<sup>26,27</sup> However, qualitatively all studies describe an approximately linear increase with increasing energy of the bombarding species and impinging-to target-mass ratio for the parameter region relevant in this study.<sup>28</sup> Taking into account the changes of magnetron power presented in the first row of Fig. 6(b), the observed evolution of deposition rate as a function of the magnetron current can be understood directly due to the changes in particle production. For Cu and W, we observe an increase in the deposition rate with an approximately linear dependence, while for Cu/37W we observe an above linear increase as a function of the magnetron current. This evolution is mostly driven by the increase in the amount of kinetic atoms arriving at the target cathode which was increased by one order of magnitude. While this would result in a strictly linear dependence, the effect of increased magnetron voltage ( $\Delta U_{mdx} \sim 40$  V from 50 mA to 500 mA) provides an additional factor due to the aforementioned increase in sputter yield. The increasing magnetron voltage is likely a result of stronger rarefaction, which indicates that the mean free path is also increasing for higher magnetron currents.<sup>29</sup>

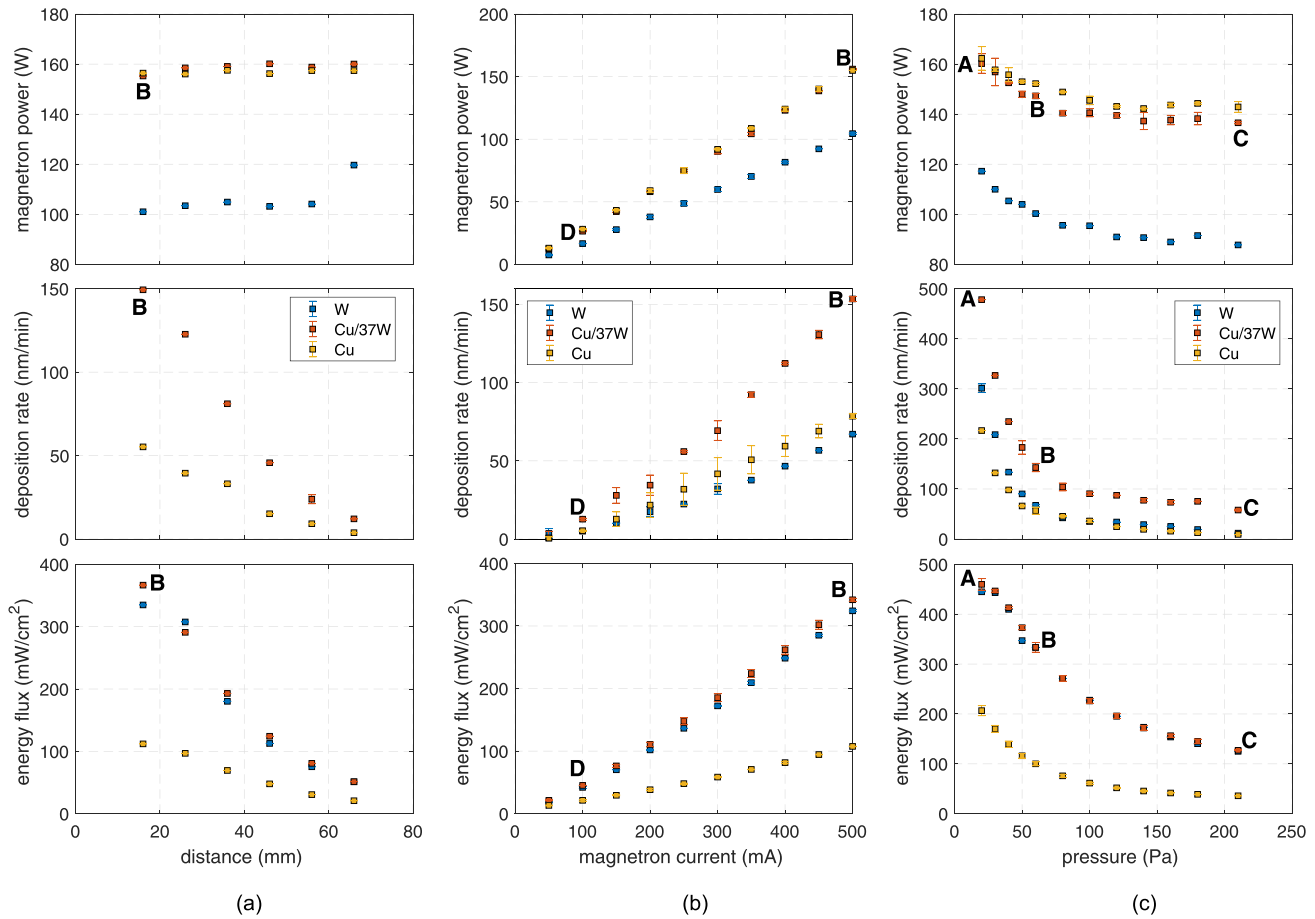


FIG. 6. Summary of the deposition rates obtained for the investigated targets and parameter variations. (a) Variation of distance between probe and target with 500 mA current and 60 Pa. Unfortunately, no distance variation while measuring the deposition rate for tungsten has been performed. (b) Variation of magnetron discharge current at 60 Pa and 16 mm distance; (c) variation of gas pressure with 500 mA current at 16 mm. Error bars obtained from repeated measurements are shown for the variation of the magnetron current (b) and argon pressure (c), although in the latter case no repeated measurements were performed with tungsten. For most conditions, the energy flux measurements showed a very good reproducibility, making the error bars smaller than the data points. The bold letters mark the data points for the corresponding SEM images (see Figs. 9 and 10) in the different conditions.

To explain the results obtained for the variation of distance and pressure [second row Figs. 6(a) and 6(c)], the transport of the species from the target to the probe surface needs to be taken into account as well. In the investigated pressure regime, the transport is strongly dominated by collisions with the background gas and with a mean free path in the sub-millimeter range; a diffusion-dominated transport can be expected. Using the common approach based on a Maxwellian gas with collisions described by the Poisson distribution, the mean free path  $\lambda_{mfp}$  for copper and tungsten in argon can be plotted as a function of the background pressure as shown in Fig. 7.<sup>30</sup> When comparing this figure to the deposition rate obtained for the pressure variation, the resemblance between the two curves suggests that the observed dependence is dominantly defined by the collision frequency of the sputtered particles with the background gas. This trend is additionally amplified by the increase in magnetron power and voltage shown in the first row of Fig. 6(c) which leads to an increased sputter yield for lower pressures.

The linear decrease for greater distances between target and probe can be directly understood as a result of the linearly increasing number of collisions the sputtered particles undergo as they drift towards the probe. While the axial drift

does not result in a decreasing flux, the diffusion perpendicular to the chamber axis and associated losses on the wall result in a decrease in the sputtered flux. For comparable systems with diffusion transport, this has been theoretically and experimentally observed by Westwood<sup>31</sup> and Ecker and Emelús.<sup>32</sup>

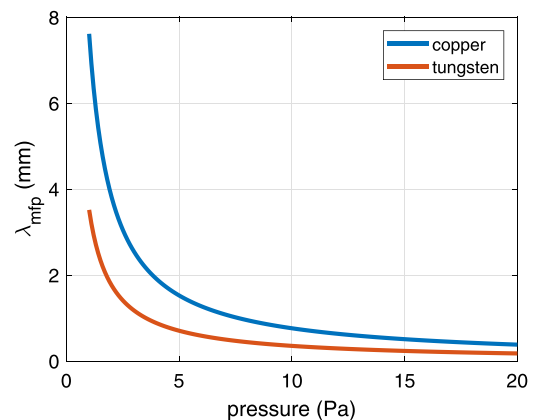


FIG. 7. Calculation of the mean free path for copper and tungsten in argon at 300 K according to kinetic gas theory.

The conspicuous deviation between the values obtained by the QCM for the compound target compared to the other two targets is not explicable from the data obtained in this study. Since separate determination of the deposition rate by sample deposition and subsequent measurement of the film thickness have not shown a strongly increased deposition rate for Cu/37W, the deviation is likely attributed to some systematic error. Similarly, the absolute QCM values for Cu and W did not match with the values obtained from sample depositions and *ex-situ* investigations that were performed for selected discharge parameters. The similarity, in spite of different sputtering yields, between copper and tungsten is thus likely attributed to systematic errors as well.

## B. Energy flux measurements

As described in Sec. III B, the energy flux obtained with the PTP is a time- and energy integrated quantity which reflects the energy flux originating from a complex set of processes.<sup>30,33</sup> In the case of magnetron sputtering in the conventional pressure regime of up to a few Pa, important contributions typically arise from the kinetic impact of particles (ions, electrons, energetic neutrals), from recombination processes at the surface or from the sublimation enthalpy which is released during film formation on the substrate. In typical DC magnetron sputtering experiments, the contributions originating from the ion-electron recombination and the kinetic flux of ions and electrons to the probe surface only contribute a few percent unless the substrate is biased to voltages significantly different from the floating potential.<sup>34,35</sup> The Langmuir measurements performed in this study resulted in ion current densities in the range of  $10^{-3}$ – $10^{-1}$  mA/cm<sup>2</sup>, maximum differences between plasma and floating potential of  $\sim 12$  V, approximate electron temperatures of around 2 eV, and electron densities of  $\sim 10^{15}$  m<sup>-3</sup>. According to the common theory described, e.g., by Kersten *et al.*<sup>36</sup> and Depla *et al.*,<sup>37</sup> the contribution due to ions and electrons can be easily calculated to be in the range of only a few mW/cm<sup>2</sup>. Considering the measured energy flux values of up to several 100 mW/cm<sup>2</sup>, the observed trends must, thus, be determined by other contributions like film condensation, kinetic neutral particles, or radiation from the plasma or the cathode, respectively.

As the pressure increases and accordingly the mean free paths of ions and neutral particles decreases to values several times smaller than the distance between substrate and cathode, an increasing amount of energy is transferred to the Ar background gas. This transfer of kinetic energy into the gas volume was investigated by Hoffman for a cylindrical magnetron sputtering source and resulted in the concept of “sputtering wind” which illustrates the directional non-uniform aspect of these energetic fluxes.<sup>38</sup> Inspired by this work, a detailed study investigating the reduction of the gas density in front of a planar magnetron cathode has been performed by Rossnagel.<sup>39</sup> Herein, the so called “rarefaction” of the gas was measured as an apparent pressure reduction and was thoroughly investigated for different combinations of gases and target materials. These investigations revealed a density reduction of up to 85% for high pressure (4 Pa) and

high magnetron power and pointed out the sputtered particles as the main driver of the gas rarefaction. Using the Monte Carlo technique, Turner<sup>40</sup> calculated similar results which coincided with the observations made by Rossnagel. From these calculations, additional parameters affecting the efficiency of the energy coupling between the sputtered and the background gas atoms have been identified. Besides the sputtering yield, the binding energy of the target material and the collision cross section and average fraction of energy transferred between sputtered particles and background gas have all been found to produce greater rarefaction for higher values. The corresponding values for the two materials used in this study are summarized in Table III.

Although the above-mentioned measurements and simulations were performed in a lower pressure regime ( $< 20$  Pa), the same principles apply in the GAS discharge investigated in this study. As mentioned above, due to the short mean free paths, we expect the sputtered flux to be thermalized within a short distance from the cathode surface. However, as demonstrated by Urbassek and Sibold, this distance is significantly underestimated if the coupling between the energetic copper particle flow and the argon background gas is neglected.<sup>44</sup> It is difficult to estimate the exact distance where the gas reaches the highest temperature or to estimate the actual mean free path; however, taking into account the obtained measurement data, we can make the following assumptions for our system:

- I. strong rarefaction with severe reduction of gas density close to the target surface,
- II. the rarefaction is dominantly driven by the sputtered metal atoms, and
- III. due to the rarefaction, the mean free path for reflected Ar neutrals is sufficiently long for them to reach the probe with high energies.

Assumptions I and II can be directly derived from the recorded magnetron power. A typical signature of rarefaction is the increase in magnetron voltage due to the increased impedance of the plasma.<sup>39</sup> From the parameters given in Table III, it can be expected that the rarefaction is more pronounced and strongest at a position much closer to the target for the cases where copper is present in the system as compared to the case where only tungsten is driving the rarefaction. This can be understood as a result of the shorter mean free path and more efficient energy exchange between the sputtered atoms and the background gas. The resulting reduction of gas density can be observed as an increase in

TABLE III. Relevant parameters for energy transfer from sputtered atoms to the background gas: sputtering yield  $Y$  for sputtering ion energy of 300 eV,<sup>41</sup> binding energy  $E_{bin}$ , collision cross-section  $\sigma$ ,<sup>30</sup> and average fraction of energy transferred from the sputtered atom per collision  $R_{te}$ .<sup>31</sup> The last column gives the energy reflection coefficient  $R_E$  of the target material for bombardment by 400 eV argon ions.<sup>42,43</sup>

	$Y$	$E_{bin}$ (eV)	$\sigma$ (nm <sup>2</sup> )	$R_{te}$	$R_E$
Cu	1.59	3.5	0.54	0.57	0.01
W	0.40	8.8	1.18	0.31	0.12

magnetron voltage and power in the first row of Fig. 6. Here, we see almost identical values for the pure copper and the composite target, while for tungsten persistently lower values are obtained. Although this could be an effect of different secondary electron yields of copper (1.3) as compared to tungsten (1.0),<sup>45</sup> this should actually result in a lower required voltage for copper as for tungsten to sustain the same current setpoint. However, Fig. 6 exhibits higher voltage values for copper which contradicts with this hypothesis and emphasizes the importance of rarefaction for the discharge parameters in this pressure regime. The similarity observed between the composite target and the pure copper target also underlines the dominance of copper as a driver of the rarefaction close to the target, and it indicates that the rarefaction close to the target is already saturated with the amount of copper available from the composite target.

Assumption III can be derived from the similarity between the energy flux of the composite and the tungsten target which is observed in all measurements in the third row of Fig. 6 and from an analysis of the possible contributions to the integral energy flux.

From the Langmuir probe measurements, it was derived that the energy flux is not strongly affected by the contribution due to electrons and ions and must, therefore, originate from other processes. The plasma radiation can also be eliminated from the list of possible origins since the typically observed values<sup>42,46</sup> are too low and the expected changes do not reflect the observed trends. Thus, the energy flux can only be attributed to the sputtered particles, to the reflected particles, or to the conduction from the heated gas.

In terms of energy flux, rarefaction can primarily be understood as a loss mechanism. Since the directed energy flux of the sputtered particles is transformed into thermal energy of the gas, the energy is transferred less directly and with losses due to the isotropic nature of the energy flux from the heated gas. In general, the maximum of gas temperature can be expected to be close to the region where the majority of the sputtered particles are thermalized. For the investigated high pressures, we expect this region to be quite close to the target, i.e., less than 16 mm away from the target. While the sputtered atoms are expected to be mostly thermalized, the longer mean free path of the fast reflected argon atoms allows them to reach the probe with a significant fraction of their initial energy. The energy flux should, thus, be a composition of the energy released during the film formation, the kinetic energy transferred upon impact of reflected argon, and the heat conducted from the hottest point of the gas towards the substrate surface. As mentioned above, this last contribution increases as a result of stronger energy losses of the sputtered atoms and is expected to be strongest for copper since the most efficient rarefaction is expected for this material. If this effect would be critical for the energy flux, we should expect, analogous to the results of the magnetron power, a similar energy flux for the copper- and the composite target. Instead, we observe a strong resemblance between the energy flux of the composite- and the tungsten target. This observation suggests that the energy flux is directly related to the presence of tungsten in the target. From Table III, it can be seen that tungsten exhibits more

than twice the binding energy of copper, which accordingly results in about twice the energy flux from film condensation per deposited atom. However, to achieve energy flux values as high as obtained here solely from the released heat of condensation, deposition rates five times the values observed in the QCM measurements would be required. Therefore, the energy deposited by the reflected argon is assumed to be the dominant contribution to the integral energy flux, especially in the cases of the composite and the tungsten target. The energy reflection coefficient  $R_E$  describes the ratio of energy reflected from the target upon impact of an ion and is given in Table III for the case of 400 eV argon ions. Due to the small mass ratio between argon and tungsten, more than 10% of the energy is reflected in the form of fast neutrals, while for copper only about 1% is reflected. From Fig. 2, it is visible that for the composite target, a high percentage of the racetrack area is made up of tungsten and we can, thus, expect a comparable amount of fast reflected particles as compared to the pure tungsten target. Taking into account the different magnetron powers, a similarly high energy flux between the two target systems can be expected. We conclude that the kinetic energy from the sputtered particles is likely dissipated by the heating of the gas and that conduction of heat through the gas only contributes a relatively small portion to the integral energy flux. The energy released during film formation is expected to contribute a considerable amount. However, it is found to be significantly smaller than the energy flux attributed to the kinetic impact of reflected neutral particles.

Since the energy flux can be understood as power transfer from the target towards the substrate, it is expected that it changes proportionally with the input power of the magnetron. If a strong change in power is present, this usually dominates the change in the energy flux as it is evident in the strong resemblance between magnetron power and energy flux for the variation of the magnetron current [see Fig. 6(b)]. Eliminating this direct proportional effect, the measurement data allow for better comparison between different systems and emphasizes other, less dominant effects. One way to achieve this is by combining the results obtained for the magnetron power  $P_{mag}$  and the energy flux  $J_s$  to calculate a value for ratio  $\eta$  of the power transfer with the following equation:

$$\eta = \frac{J_s}{P_{mag}/A_{mag}}, \quad (4)$$

with  $A_{mag}$  being the target surface area. Such normalized results are summarized in Fig. 8.

After taking into account the increased magnetron power for Cu and Cu/37W, tungsten exhibits the highest energy flux values compared to the other two targets in all variation runs (see Fig. 8). A similar difference in energy flux between Cu and W has been observed by Harbauer *et al.*<sup>47</sup> in the conventional lower pressure regime. Although they observed three times higher deposition rates for copper as compared to tungsten, they obtained three times higher values for the energy flux for tungsten, which was argued to likely be a result of the higher heat of condensation (8.8 eV

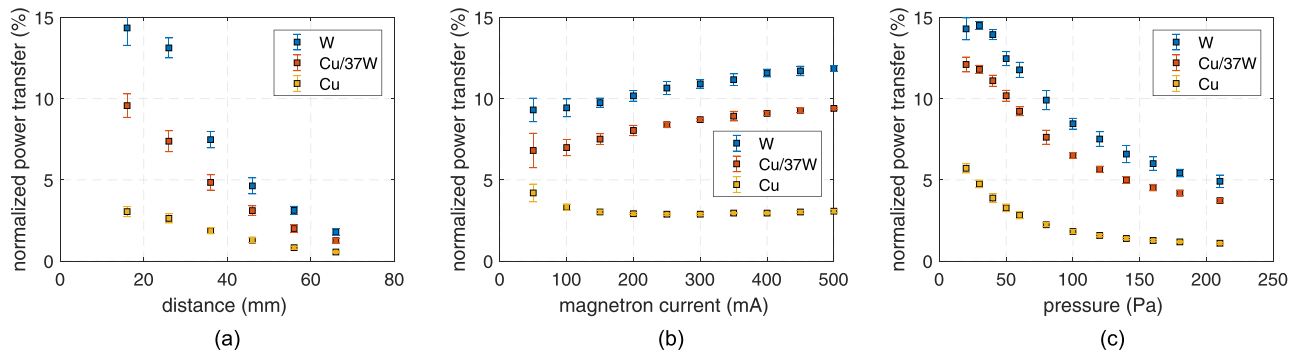


FIG. 8. Summary of PTP results normalized with the magnetron power according to Eq. (4). (a) Variation of distance between probe and target with 500 mA current and 60 Pa, (b) variation of magnetron discharge current at 60 Pa and 16 mm distance, and (c) variation of gas pressure with 500 mA current at 16 mm.

for W, 3.5 eV for Cu<sup>48</sup>) Thornton *et al.*<sup>46,49</sup> obtained similar results from their investigations of the energy flux per deposited atom. They found that the energy transfer per deposited particle of tungsten yields about eight times the one obtained for copper. In addition to the aforementioned higher heat of condensation, Thornton points out the importance of reflected argon atoms with energies up to the cathode potential as an important contribution.

Although these investigations were done at a pressure of roughly 1 Pa, the findings coincide with our results shown in Fig. 8 and, thus, they further support the assumption that the relevant contributions to the integral energy flux in the higher pressure regime of 20–210 Pa are similar to the ones found in the conventional pressure regime.

Albeit, as argued in Sec. III A, the absolute values obtained for the deposition rate likely exhibit a significant systematic error; for the sake of comparison, we shall use them here to obtain an estimate for the obtained energy per deposited atom. For example, for the variation of the magnetron current, we calculate relatively constant energies per atom of  $\sim 500$  eV for tungsten and  $\sim 100$  eV and  $\sim 150$  eV for pure copper and the composite target, respectively. As argued above, these values are too high to be only a result of film deposition, but are most likely attributed to the impact of reflected neutrals and heat conduction through the gas. Compared to the values obtained by Thornton *et al.*, our values are approximately 5 times higher and compared to Drüsedau *et al.*,<sup>42</sup> they are 2.5 times higher. In agreement with the observations by Drüsedau who observed a linear increase in the energy per atom in the pressure regime from 0.1 to 10 Pa, we observed a comparable increase for pressures below 60 Pa. Taking this trend into account, the higher values obtained in this study fit reasonably well with the results obtained by the studies in the conventional pressure regime. Drüsedau also supports the assumption that reflected neutrals play a significant role as a part to the energy flux since they calculated the fast neutrals to account for roughly 75% of the energy per atom in the case of tungsten [Fig. 9(b) in Ref. 42].

The observation that the composite target exhibits slightly lower normalized energy flux values than the pure tungsten can be understood as a combination of the smaller contribution from film formation due to the smaller binding energy of copper and a reduction of the contribution from

reflected neutrals as a result of the reduced race track area covered by tungsten.

### C. SEM investigations

To investigate the effect of the different energy flux values on film formation and to compare them to the well-established structure zone model, additional investigations have been performed by an *ex-situ* study of four deposited films using the composite target at a substrate distance of 16 mm. Three films were deposited with 500 mA and pressures of  $p = 20$  Pa,  $p = 60$  Pa and  $p = 210$  Pa and one film was deposited with a lower current of 100 mA at 60 Pa. The deposited films have been investigated using a scanning electron microscope (SEM) and are presented in Figs. 9 and 10.

In Fig. 9, it can be seen that the sample for the lowest pressure (20 Pa) exhibits a structure as it is known from common film growth. The columnar growth appears to be significantly disrupted by particles and less organized for 60 Pa and at 210 Pa the film appears to be completely composed of bigger particles. Comparing the structure observed for the 20 Pa sample to the structure zone diagram (SZD) by Thornton<sup>50</sup> or Movchan and Demchishin,<sup>51</sup> we find a zone 1 structure which was observed by Thornton for the highest investigated

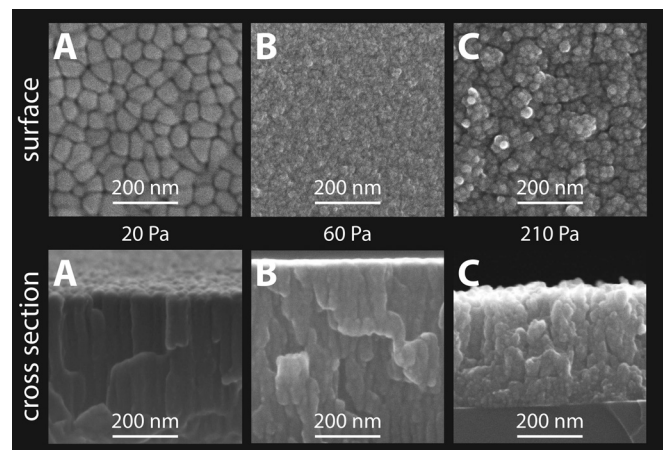


FIG. 9. SEM images of deposited film structures using the Cu/37W composite target. The first row shows top view images of the film surface and the second row shows cross sections revealing the growth structure. All depositions were performed at a distance of  $d = 16$  mm and a magnetron current of  $I_{mag} = 500$  mA. The bold letters correlate to the letters in Fig. 6, indicating the corresponding magnetron power, deposition rate, and energy flux.

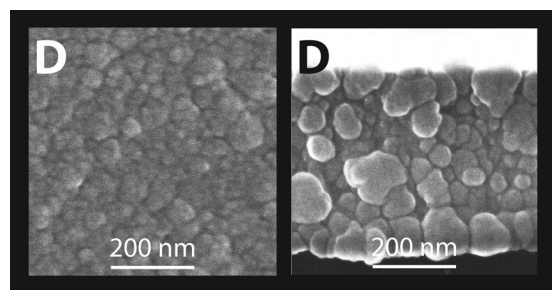


FIG. 10. SEM images of deposited film structures using the Cu/37W composite target in 60 Pa at a magnetron current of 100 mA. The left image shows the surface and the right one a cross section of the film. The bold letters correlate to the letters in Fig. 6, indicating the corresponding magnetron power, deposition rate and energy flux.

pressures ( $\sim 4$  Pa) or at low substrate temperatures independent of the pressure. The surface exhibits tapered crystallites separated by voids, and the structural growth direction is characterized by the incoming particle flux.

Similar to the case for 210 Pa (C), for condition of 100 mA magnetron current and 60 Pa pressure (D), we find a film which is completely composed of particles as shown in Fig. 10. However, now the particles exhibit a distinctively different form and size. While in C the film appears to be formed from relatively evenly sized  $\sim 20$  nm particles or clusters of those particles, in D we find a variety of different particles with smooth surfaces and sizes ranging from  $\sim 20$  nm to 100 nm. This difference indicates that the particles in D were formed at a lower rate by surface growth (attachment of single atoms), whereas the particles in C are likely formed by cluster-cluster collisions. Taking into account the more structured film obtained in B at the same pressure of D but at a significantly higher magnetron current, the role of rarefaction and initial energy of the sputtered atoms for the NP formation becomes apparent.

## V. CONCLUSIONS

Although gas aggregation cluster sources are usually operated in higher pressure regimes than conventional DC magnetron sputtering systems, the basic mechanisms contributing to the integral energy flux are comparable. The current study confirms that contributions from charged particles (i.e., electrons and ions) and radiation have comparably small influences on the integral energy flux. Similar to the conventional low pressure sputtering regime, the integral energy flux is mainly driven by the contribution due to film condensation and reflected neutrals, with the latter being strongly dependent on the mass ratio between gas and target atoms. This was especially evident in the strong resemblance observed in the energy flux between the pure tungsten and the composite target. Gas rarefaction and its accompanying effects were argued to be a significant mechanism in the investigated system as the reduction of the gas density and the associated increase in  $\lambda_{mfp}$  allowed the reflected neutrals to reach the substrate surface with high energies creating a significant contribution to the energy flux.

## ACKNOWLEDGMENTS

This work was partially funded by GACR 17-22016S from the Grant Agency of the Czech Republic.

- <sup>1</sup>C. Binns, "Nanoclusters deposited on surfaces," *Surf. Sci. Rep.* **44**, 1–49 (2001).
- <sup>2</sup>K. Wegner, P. Piseri, H. V. Tafreshi, and P. Milani, "Cluster beam deposition: A tool for nanoscale science and technology," *J. Phys. D: Appl. Phys.* **39**, R439–R459 (2006).
- <sup>3</sup>C. Cassidy, V. Singh, P. Grammatikopoulos, F. Djurabekova, K. Nordlund, and M. Sowwan, "Inoculation of silicon nanoparticles with silver atoms," *Sci. Rep.* **3**, 3083 (2013).
- <sup>4</sup>P. Solař, I. Melnichuk, A. Artemenko, O. Polonskyi, O. Kylián, A. Choukourov, D. Slavínská, and H. Biederman, "Nylon-sputtered plasma polymer particles produced by a semi-hollow cathode gas aggregation source," *Vacuum* **111**, 124–130 (2015).
- <sup>5</sup>U. R. Kortshagen, R. M. Sankaran, R. N. Pereira, S. L. Girshick, J. J. Wu, and E. S. Aydil, "Nonthermal plasma synthesis of nanocrystals: Fundamental principles, materials, and applications," *Chem. Rev.* **116**, 11061–11127 (2016).
- <sup>6</sup>K. Sattler, J. Mühlbach, and E. Recknagel, "Generation of metal clusters containing from 2 to 500 atoms," *Phys. Rev. Lett.* **45**, 821–824 (1980).
- <sup>7</sup>H. Haberland, M. Karrais, M. Mall, and Y. Thurner, "Thin films from energetic cluster impact: A feasibility study," *J. Vac. Sci. Technol., A* **10**, 3266–3271 (1992).
- <sup>8</sup>T. Takagi, "Ionized cluster beam (ICB) deposition and processes," *Pure Appl. Chem.* **60**, 781–794 (1988).
- <sup>9</sup>O. Polonskyi, T. Peter, A. Mohammad Ahadi, A. Hinz, T. Strunskus, V. Zaporozhchenko, H. Biederman, and F. Faupel, "Huge increase in gas phase nanoparticle generation by pulsed direct current sputtering in a reactive gas admixture," *Appl. Phys. Lett.* **103**, 033118 (2013).
- <sup>10</sup>B. M. Smirnov, I. Shyjumon, and R. Hippler, "Flow of nanosize cluster-containing plasma in a magnetron discharge," *Phys. Rev. E* **75**, 066402 (2007).
- <sup>11</sup>J. Kousal, O. Polonskyi, O. Kylián, A. Choukourov, A. Artemenko, J. Pešička, D. Slavínská, and H. Biederman, "Characterization of nanoparticle flow produced by gas aggregation source," *Vacuum* **96**, 32–38 (2013).
- <sup>12</sup>P. A. Skovorodko, S. A. Brown, and D. Belić, "Gas dynamic considerations for performance of nanocluster deposition system," *AIP Conf. Proc.* **1333**, 203–208 (2011).
- <sup>13</sup>J. Hanuš, M. Vaidulych, O. Kylián, A. Choukourov, J. Kousal, I. Khalakhan, M. Cieslar, P. Solař, and H. Biederman, "Fabrication of Ni@Ti core-shell nanoparticles by modified gas aggregation source," *J. Phys. D: Appl. Phys.* **50**, 475307 (2017).
- <sup>14</sup>A. Caillard, S. Cuynet, T. Lecas, P. Andreatza, M. Mikikian, A.-L. Thomann, and P. Brault, "PdPt catalyst synthesized using a gas aggregation source and magnetron sputtering for fuel cell electrodes," *J. Phys. D: Appl. Phys.* **48**, 475302 (2015).
- <sup>15</sup>M. Benelmekki, J. Vernieres, J.-H. Kim, R.-E. Diaz, P. Grammatikopoulos, and M. Sowwan, "On the formation of ternary metallic-dielectric multicore-shell nanoparticles by inert-gas condensation method," *Mater. Chem. Phys.* **151**, 275–281 (2015).
- <sup>16</sup>M. Tchapyguine, T. Andersson, C. Zhang, and O. Björneholm, "Core-shell structure disclosed in self-assembled Cu-Ag nanoalloy particles," *J. Chem. Phys.* **138**, 104303 (2013).
- <sup>17</sup>G. Krishnan, M. A. Verheijen, G. H. ten Brink, G. Palasantzas, and B. J. Kooi, "Tuning structural motifs and alloying of bulk immiscible Mo—Cu bimetallic nanoparticles by gas-phase synthesis," *Nanoscale* **5**(12), 5375 (2013).
- <sup>18</sup>A. Vahl, J. Strobel, W. Reichstein, O. Polonskyi, T. Strunskus, L. Kienle, and F. Faupel, "Single target sputter deposition of alloy nanoparticles with adjustable composition via a gas aggregation cluster source," *Nanotechnology* **28**, 175703 (2017).
- <sup>19</sup>E. Pérez-Tijerina, M. Gracia Pinilla, S. Mejía-Rosales, U. Ortiz-Méndez, A. Torres, and M. José-Yacamán, "Highly size-controlled synthesis of Au/Pd nanoparticles by inert-gas condensation," *Faraday Discuss.* **138**, 353–362 (2008).
- <sup>20</sup>V. M. Serdio, M. A. Gracia-Pinilla, S. Velumani, E. G. Pérez-Tijerina, and W. van der Weil, "Synthesis and characterization of NiCr self-assembled nanorings," *J. Nano Res.* **9**, 101–108 (2010).
- <sup>21</sup>R. Wang, O. Dmitrieva, M. Farle, G. Dumpich, M. Acet, S. Mejía-Rosales, E. Perez-Tijerina, M. J. Yacamán, and C. Kisielowski, "FePt

- Icosahedra with magnetic cores and catalytic shells," *J. Phys. Chem. C* **113**, 4395–4400 (2009).
- <sup>22</sup>P. Solař, D. Nikitin, J. Hanuš, O. Kylián, M. Vaidulych, M. Cieslar, H. Valentova, and H. Biederman, "Production of heterogenous copper-tungsten particles," in Proceedings of the Nanocon (Brno) (2017).
- <sup>23</sup>Intelmetrics Global Ltd., *Model IL150 Thickness Monitor - Instruction Manual*.
- <sup>24</sup>M. Stahl, T. Trottenberg, and H. Kersten, "A calorimetric probe for plasma diagnostics," *Rev. Sci. Instrum.* **81**(2), 023504 (2010).
- <sup>25</sup>S. Gauter, M. Fröhlich, W. Garkas, M. Polak, and H. Kersten, "Calorimetric probe measurements for a high voltage pulsed substrate (PBII) in a HiPIMS process," *Plasma Sources Sci. Technol.* **26**, 065013 (2017).
- <sup>26</sup>P. C. Zalm, "Energy dependence of the sputtering yield of silicon bombarded with neon, argon, krypton, and xenon ions," *J. Appl. Phys.* **54**, 2660–2666 (1983).
- <sup>27</sup>P. Sigmund, "Elements of sputtering theory," *Nanofabrication by Ion-Beam Sputtering* (Pan Stanford Publishing, 2012), pp. 1–40.
- <sup>28</sup>P. Sigmund, "Theory of sputtering. I. Sputtering yield of amorphous and polycrystalline targets," *Phys. Rev.* **184**, 383–416 (1969).
- <sup>29</sup>S. M. Rossnagel and H. R. Kaufman, "Charge transport in magnetrons," *J. Vac. Sci. Technol., A* **5**, 2276–2279 (1987).
- <sup>30</sup>*Reactive Sputter Deposition*, Springer Series in Materials Science Vol. 109, D. Depla and S. Mahieu (Springer, Berlin/Heidelberg, 2008).
- <sup>31</sup>W. D. Westwood, "Calculation of deposition rates in diode sputtering systems," *J. Vac. Sci. Technol.* **15**, 1–9 (1978).
- <sup>32</sup>G. Ecker and K. G. Emeléus, "Cathode sputtering in glow discharges," *Proc. Phys. Soc., Sect. B* **67**, 546–552 (1954).
- <sup>33</sup>H. Kersten, H. Deutsch, H. Steffen, G. Kroesen, and R. Hippler, "The energy balance at substrate surfaces during plasma processing," *Vacuum* **63**, 385–431 (2001).
- <sup>34</sup>R. Wendt, K. Ellmer, and K. Wiesemann, "Thermal power at a substrate during ZnO:Al thin film deposition in a planar magnetron sputtering system," *J. Appl. Phys.* **82**, 2115–2122 (1997).
- <sup>35</sup>D. Rohde, P. Pecher, H. Kersten, W. Jacob, and R. Hippler, "The energy influx during plasma deposition of amorphous hydrogenated carbon films," *Surf. Coat. Technol.* **149**(2-3), 206–216 (2002).
- <sup>36</sup>H. Kersten, D. Rohde, H. Steffen, H. Deutsch, R. Hippler, G. H. P. M. Swinkels, and G. M. W. Kroesen, "On the determination of energy fluxes at plasma—surface processes," *Appl. Phys. A* **72**(5), 531–540 (2001).
- <sup>37</sup>D. Depla, S. Heirwegh, S. Mahieu, J. Haemers, and R. De Gryse, "Understanding the discharge voltage behavior during reactive sputtering of oxides," *J. Appl. Phys.* **101**, 013301 (2007).
- <sup>38</sup>D. W. Hoffman, "A sputtering wind," *J. Vac. Sci. Technol., A* **3**, 561–566 (1985).
- <sup>39</sup>S. M. Rossnagel, "Gas density reduction effects in magnetrons," *J. Vac. Sci. Technol., A* **6**(1), 19 (1988).
- <sup>40</sup>G. M. Turner, "Monte Carlo calculations of gas rarefaction in a magnetron sputtering discharge," *J. Vac. Sci. Technol., A* **13**, 2161–2169 (1995).
- <sup>41</sup>N. Laegreid and G. K. Wehner, "Sputtering yields of metals for Ar + and Ne + ions with energies from 50 to 600 eV," *J. Appl. Phys.* **32**, 365–369 (1961).
- <sup>42</sup>T. P. Drüsedau, T. Bock, T.-M. John, F. Klabunde, and W. Eckstein, "Energy transfer into the growing film during sputter deposition: An investigation by calorimetric measurements and Monte Carlo simulations," *J. Vac. Sci. Technol., A* **17**, 2896–2905 (1999).
- <sup>43</sup>W. Eckstein and J. P. Biersack, "Reflection of heavy ions," *Z. Phys. B: Condens. Matter* **63**, 471–478 (1986).
- <sup>44</sup>H. M. Urbassek and D. Sibold, "Sputtered atom transport in high-current gas discharges: A self-consistent computer simulation study," *J. Vac. Sci. Technol., A* **11**, 676–681 (1993).
- <sup>45</sup>R. L. Petry, "Secondary electron emission from tungsten, copper and gold," *Phys. Rev.* **28**, 362–366 (1926).
- <sup>46</sup>J. A. Thornton, "Substrate heating in cylindrical magnetron sputtering sources," *Thin Solid Films* **54**(1), 23–31 (1978).
- <sup>47</sup>K. Harbauer, T. Welzel, and K. Ellmer, "A combined sensor for the diagnostics of plasma and film properties in magnetron sputtering processes," *Thin Solid Films* **520**(20), 6429–6433 (2012).
- <sup>48</sup>W. M. Haynes, *CRC Handbook of Chemistry and Physics* (CRC Press, Boca Raton, FL, 2014).
- <sup>49</sup>J. A. Thornton and J. L. Lamb, "Substrate heating rates for planar and cylindrical-post magnetron sputtering sources," *Thin Solid Films* **119**, 87–95 (1984).
- <sup>50</sup>J. A. Thornton, "Influence of apparatus geometry and deposition conditions on the structure and topography of thick sputtered coatings," *J. Vac. Sci. Technol.* **11**(4), 666 (1974).
- <sup>51</sup>B. A. Movchan and A. V. Demshishin, "Study of the structure and properties of thick vacuum condensates of nickel, titanium, tungsten, aluminum oxide and zirconium dioxide," *Phys. Met. Metallogr.* **28**, 83–90 (1969).